Supporting Information

Linear Optical Afterglow and Nonlinear Optical Harmonic Generation from Chiral Tin(IV) Halides: the Role of Lattice Distortions

Xiao Han, Puxing Chen, Rongchao Shi, Yongshen Zheng, Siming Qi, Jialiang Xu* and Xian-He Bu

X. Han, P. Chen. Prof. J. Xu, Prof. X.-H. Bu.
School of Materials Science and Engineering
Smart Sensing Interdisciplinary Science Center
Collaborative Innovation Center of Chemical Science and Engineering (Tianjin)
Nankai University
Tongyan Road 38, Tianjin 300350, P. R. China
E-mail: jialiang.xu@nankai.edu.cn

Table of Contents

Experimental Procedures

Materials. Tin (IV) chloride pentahydrate ($SnCl_4 \cdot 5H_2O$, Energy Chemical, 99%), hydrochloric acid (HCl, Aladdin, 36 wt%. in water), *R*-methyl(4-fluorobenzyl)amine (*R*-FMBA, Bidepharm, 98%), *S*-methyl(4-fluorobenzyl)amine (*S*-FMBA, Bidepharm, 98%), *rac*-methyl(4-fluorobenzyl)amine (*rac*-FMBA, Bidepharm, 98%), *R*-methyl(4-chlorobenzyl)amine (*R*-ClMBA, Bidepharm, 98%), *S*-methyl(4-chlorobenzyl)amine (*S*-ClMBA, Bidepharm, 98%), *rac*-methyl(4-chlorobenzyl)amine (*rac*-ClMBA, Bidepharm, 98%). Chemicals listed above are commercially available and used without further purification.

Synthesis and crystal growth. In double-neck flask,1 mmol *R*-, *S*- or *rac*-XMBA (X = F, Cl) and 0.5 mmol $SnCl_4 \cdot 5H_2O$ were added into 5-7 mL HCl solution to form white precipitation. A colorless clear solution was obtained after continual heating and stirring. Then the solution cooled to the room temperature slowly and the target crystals were formed. Subsequently, the crystals should be filtered and washed with *n*-hexane, and thoroughly dried in vacuum drying oven.

Characterization. Single-crystal X-ray diffraction data of *R*-, *S*- or *rac*-XMBA (X = F, Cl) were collected using a Rigaku XtaLAB MM007 CCD diffractometer with Mo Kα radiation (λ= 0.71073 Å) at 100 K. The structures of crystals were solved and refined using Olex2[1]. Powder X-ray diffraction (PXRD) spectra were recorded on a Rigaku D/Max-2500 diffractometer at 40 kV, 100 mA with a Cu-target tube and a graphite monochromator. Thermogravimetric analyses (TGA) were carried out with a standard TG–DTA analyzer under air atmosphere at a heating rate of 10 °C/min, with an empty Al_2O_3 crucible used as reference. UV–vis spectra were performed on a Cary 100conc spectrophotometer. X-ray photoelectron spectra (XPS) were carried out on a Thermo Scientific ESCALAB 250Xi with Al Kα radiation. The binding energy was calibrated using the C 1s photoelectron peak at 284.6 eV as the reference. UV–vis absorbance spectra and UV–vis–NIR spectra were recorded with UV 2600 and PerkinElmer LAMBDA 1050, respectively. The linear circular dichroism (CD) spectra were collected using BioLogic MOS-450 CD spectrometer in a transmission geometry. Edinburgh FS5 fluorescence spectrometer was applied to collect the luminescence spectra, lifetimes and quantum yields. Luminescent decay experiments were measured on an Edinburgh FS5 spectrometer using time-correlated single photon counting (TCSPC)The PL absolute quantum yields were defined as the number of photons emitted per photon absorbed by the systems and measured with an integrating sphere.

Nonlinear optical measurements. The nonlinear optical (NLO) measurements were conducted using a home-built multiphoton nonlinear optical microscope system. Briefly, a commercial femotosecond pump (Mai Tai HP, <100 fs, 80 MHZ, wavelength ranging from 690 to 1040 nm) in reflection geometry. A laser beam is incident on the samples with an incident angle γ (γ = 45˚) and the generated SHG signals are collected in the reflection configuration. The linearly polarized pump was altered with the λ/2 plate. The second-order NLO susceptibility of the samples was determined by using Y-cut quartz and urea crystal as the reference.

DFT calculations. The DFT calculations were implemented in Vienna Ab initio Simulation Package (VASP 5.4.4) adopting the projector augmented-wave method (PAW) to deal with the ion-electron interaction[2, 3]. We selected the generalized gradient approximation (GGA) of Perdew-Burke-Ernzerhof (PBE) to approximate the exchange-correlation energy[4]. Considering the nonbonding and long-range interaction in the hybrid organic-inorganic metal halides, the van der Waals (vdW) correction (DFT-D3) was adopted in the calculations[5]. The plane-wave basis set was defined by the energy cut-off at 520 eV. The energy convergence criterion for electronic iteration was set to be 10-5 eV. The structural relaxation was performed until the Hellmann-Feynman forces on each atom are less than 0.01 eV/Å. A Γ-centered 3 × 6 × 3 grid was adopted to simulate the k-space integrations. To obtain reasonable electronic bandgaps, the Heyd-Scuseria-Ernzerhof (HSE) hybrid density functional calculations are also performed[6].

Quantification of the second-order NLO coefficient (d_{eff}). The SHG signal reflected from the front surface of crystals and quartz reference has been collected for the determination of second-order NLO coefficient. The polarization of the incident light and the reflected SHG signal of both samples and Y-cut quartz are *p*-polarized. We assume that the birefringence is negligible and the refractive index of air is 1. The electric field of reflected SHG intensity of the front surface can be calculated by the equation:

$$E_{rp} = \frac{n(\omega)\cos\theta - n(2\omega)\cos\theta_t}{\cos\theta + n(2\omega)\cos\theta_r} \cdot \frac{P_{NLp}^{(2)}}{\varepsilon_0(n(\omega)^2 - n(2\omega)^2)} + \frac{n(2\omega)\sin\theta_t}{\cos\theta + n(2\omega)\cos\theta_r} \cdot \frac{P_{NLt}^{(2)}}{\varepsilon_0 n(2\omega)^2} \qquad \text{* MERGEFORMAT (S1)}$$

where $P_{NLp}^{(2)}$ is the second-order nonlinear polarization parallel to the *p*-polarization of the transmitted fundamental wavelength and $P_{NLt}^{(2)}$ is the second-order nonlinear polarization parallel to the direction of the transmitted fundamental wavelength propagation, $n(\omega)$ and $n(2\omega)$ are the of refractive indexes of the sample at the fundamental wavelength and the SHG wavelength, respectively. θ_r is the reflection angle, which is equal to the incident angle θ_i , θ_t is the refraction angle of fundamental wavelength and θ is the angle of the SHG in bulk. These angles can be calculated by the following formula:

$$n(\omega)\sin\theta_t = n(2\omega)\sin\theta = \sin\theta_r = \sin\theta_i \qquad \text{* MERGEFORMAT (S2)}$$

For quartz, there are two independent NLO susceptibility elements.

$$\beta_{xxx} = -\beta_{xyy} = -\beta_{yxy} = -\beta_{yyx} = \beta_1 \qquad \text{* MERGEFORMAT (S3)}$$

$$\beta_{xyz} = \beta_{xzy} = -\beta_{yxz} = -\beta_{yzx} = \beta_2 \qquad \text{* MERGEFORMAT (S4)}$$

Here, β is NLO susceptibility of quartz. $\beta_2 \approx 0.02\,\beta_1$, and β_2 is usually negligible. In the experiment, Y-cut quartz is used as a reference and the Z-axis is vertical to the optical table. $P_{NLp}^{(2)}$ and $P_{NLt}^{(2)}$ can be described as:

$$P_{NLp,quartz}^{(2)} = -\varepsilon_0((E_x^{\,2} - E_y^{\,2})\cos\theta_t + 2E_xE_y\sin\theta_t)\beta_1 \qquad \text{* MERGEFORMAT (S5)}$$

$$P^{(2)}_{NLt,quartz} = \varepsilon_0((E_x^{\ 2} - E_y^{\ 2})\sin\theta_t - 2E_xE_y\cos\theta_t)\beta_1 \qquad \text{* MERGEFORMAT (S6)}$$

E_x and E_y are the electric field of the fundamental wavelength in quartz. E_x and E_y can be described by Fresnel formulae:

$$E_x = \frac{2\cos\theta_i\cos\theta_t}{\cos\theta_t + n\cos\theta_i}E_i \qquad \text{* MERGEFORMAT (S7)}$$

$$E_y = -\frac{2\cos\theta_i\sin\theta_t}{\cos\theta_t + n\cos\theta_i}E_i \qquad \text{* MERGEFORMAT (S8)}$$

$n_{quartz}(980\text{ nm}) = 1.481$ and $n_{quartz}(490\text{ nm}) = 1.497$; $\theta_i = \theta_r = 45^\circ$. So that $\theta = 28.19^\circ$ and $\theta_t = 28.52^\circ$

$$E_{rp,quartz} = 0.0884\beta_1E_i^{\ 2} \qquad \text{* MERGEFORMAT (S9)}$$

For samples, we assumed that the $P^{(2)}_{NLt}$ is negligible and

$$P^{(2)}_{NLP,samp} = \varepsilon_0 d_{eff}E_p^{\ 2} \qquad \text{* MERGEFORMAT (S10)}$$

$$E_p = \frac{2\cos\theta_i}{\cos\theta_t + n\cos\theta_i}E_i \qquad \text{* MERGEFORMAT (S11)}$$

$n_{samp}(980\text{ nm}) = 1.639$ and $n_{samp}(490\text{ nm}) = 1.632$; $\theta_i = \theta_r = 45^\circ$. So that $\theta = 28.19^\circ$ and $\theta_t = 28.52^\circ$

$$E_{rp,samp} = 0.0440d_{eff}E_i^{\ 2} \qquad \text{* MERGEFORMAT (S12)}$$

$$\frac{I_{samp}}{I_{quartz}} = \left|\frac{E_{rp,samp}}{E_{rp,quartz}}\right|^2 = \left|\frac{d_{eff}E_i^{\ 2}}{\beta_1E_i^{\ 2}}\right|^2 \qquad \text{* MERGEFORMAT (S13)}$$

$\frac{I_{samp}}{I_{quartz}} = 796$, the second-order nonlinear susceptibility of Y-cut quartz plate, i.e., β_1, is assumed to be 0.6 pm V^{-1}[17, 8].

Thus, $d_{eff}^{\ s}$ of ***S*-Cl** at 980 nm can be calculated: d_{eff} =18.8 pmV^{-1}.

Supplementary Tables

Table S1. Crystallographic data and structure refinement details for ***R*-Cl**, ***S*-Cl** and ***rac*-Cl**.

Identification code	***R*-Cl**	***S*-Cl**	***rac*-Cl**
Empirical formula	$C_{16}H_{22}Cl_8N_2Sn$	$C_{16}H_{22}Cl_8N_2Sn$	$C_{16}H_{22}Cl_8N_2Sn$
Formula weight	644.64	644.64	644.64
Temperature/K	100	100	100
Crystal system	monoclinic	monoclinic	monoclinic
Space group	$P2_1$	$P2_1$	$P2_1/c$
a/Å	12.2599(3)	12.2556(2)	14.1247(2)
b/Å	7.1234(2)	7.10740(10)	7.10940(10)
c/Å	14.1245(3)	14.0867(3)	12.3083(2)
α/°	90	90	90
β/°	98.056(2)	98.156(2)	97.523(10)
γ/°	90	90	90
Volume/Å^3	1221.35(5)	1214.62(4)	1225.34(3)
Z	2	2	2
ρ_{calc}g/cm^3	1.753	1.763	1.747
μ/mm^{-1}	1.928	1.938	16.374
F(000)	636.0	636.0	636.0
Reflections collected	25373	19109	7233
Data/restraints/parameters	6930/1/248	6331/1/248	2470/0/126
Goodness-of-fit on F^2	1.050	1.035	1.181
Final R indexes [I>=2σ (I)]	R_1 = 0.0206, wR_2 = 0.0434	R_1 = 0.0160, wR_2 = 0.0362	R_1 = 0.0723,wR_2 = 0.1945
Final R indexes [all data]	R_1 = 0.0231, wR_2 = 0.0441	R_1 = 0.0166, wR_2 = 0.0364	R_1 = 0.0736,wR_2 = 0.1956
Flack parameter	-0.019(10)	-0.040(8)	-0.035(12)
CCDC	2207677	2207676	2210696

Table S2. Selected bond lengths (Å) for ***R*-Cl**, ***S*-Cl** and ***rac*-Cl**.

***R*-Cl**		***S*-Cl**		***rac*-Cl**	
Sn1-Cl1	2.4158(7)	Sn1-Cl5	2.4169(6)	Sn1-Cl3	2.4212(17)
Sn1-Cl6	2.4600(7)	Sn1-Cl4	2.4614(6)	Sn1-Cl3	2.4212(17)
Sn1-Cl4	2.4153(6)	Sn1-Cl7	2.4364(5)	Sn1-Cl2	2.4306(18)
Sn1-Cl3	2.4313(7)	Sn1-Cl3	2.4143(5)	Sn1-Cl2	2.4305(18)
Sn1-Cl2	2.4358(6)	Sn1-Cl8	2.4339(6)	Sn1-Cl1	2.4243(18)
Sn1-Cl5	2.4126(7)	Sn1-Cl6	2.4130(6)	Sn1-Cl1	2.4243(18)
Cl8-C8	1.743(3)	Cl1-C2	1.744(2)	Cl4-C6	1.740(8)
Cl7-C1	1.745(3)	Cl2-C10	1.744(2)	C6-C7	1.367(13)
N1-C7	1.516(3)	N2-C15	1.521(3)	N1-C2	1.478(12)
N2-C14	1.511(3)	N1-C7	1.515(3)	C6-C5	1.397(12)

Table S3. Selected bond angles (°) for ***R*-Cl**, ***S*-Cl** and ***rac*-Cl**.

***R*-Cl**		***S*-Cl**		***rac*-Cl**	
Cl1-Sn1-Cl6	87.23(2)	Cl5-Sn1-Cl4	87.30(2)	Cl3-Sn1-Cl3	180.0
Cl1-Sn1-Cl3	176.75(3)	Cl5-Sn1-Cl7	90.70(2)	Cl3-Sn1-Cl2	88.68(6)
Cl1-Sn1-Cl2	90.76(3)	Cl5-Sn1-Cl8	176.62(2)	Cl3-Sn1-Cl2	91.32(6)
Cl4-Sn1-Cl1	89.88(3)	Cl7-Sn1-Cl4	89.36(2)	Cl3-Sn1-Cl2	91.31(6)
Cl4-Sn1-Cl6	90.63(3)	Cl3-Sn1-Cl5	89.90(2)	Cl3-Sn1-Cl2	88.69(6)
Cl4-Sn1-Cl3	90.85(3)	Cl3-Sn1-Cl4	90.68(2)	Cl3-Sn1-Cl1	90.72(6)
Cl4-Sn1-Cl2	179.36(4)	Cl3-Sn1-Cl7	179.39(3)	Cl3-Sn1-Cl1	90.71(6)
Cl3-Sn1-Cl6	89.59(3)	Cl3-Sn1-Cl8	90.89(2)	Cl3-Sn1-Cl1	89.29(6)
Cl3-Sn1-Cl2	88.52(3)	Cl8-Sn1-Cl4	89.40(2)	Cl3-Sn1-Cl1	89.29(6)
Cl2-Sn1-Cl6	89.47(3)	Cl8-Sn1-Cl7	88.50(2)	Cl2-Sn1-Cl2	180.0
Cl5-Sn1-Cl1	93.22(3)	Cl6-Sn1-Cl5	93.19(2)	Cl1-Sn1-Cl2	89.98(7)
Cl5-Sn1-Cl6	179.24(3)	Cl6-Sn1-Cl4	179.15(2)	Cl1-Sn1-Cl2	90.02(7)
Cl5-Sn1-Cl4	89.98(3)	Cl6-Sn1-Cl7	89.95(2)	Cl1-Sn1-Cl2	90.02(7)
Cl5-Sn1-Cl3	89.95(3)	Cl6-Sn1-Cl3	90.01(2)	Cl1-Sn1-Cl2	89.98(7)
Cl3-Sn1-Cl2	89.91(3)	Cl4-Sn1-Cl8	90.10(2)	Cl1-Sn1-Cl1	180.00(8)

C2-C1-Cl7	119.7(3)	C3-C2-Cl1	119.6(2)	C7-C6-Cl4	119.6(3)
C6-C1-Cl7	118.6(3)	C1-C2-Cl1	118.9(2)	C5-C6-Cl4	118.5(3)
C13-C8-Cl8	119.5(3)	C9-C10-Cl2	119.8(2)	C7-C6-C5	122.1(8)
C9-C8-Cl8	119.1(3)	C11-C10-Cl2	118.7(2)	C8-C7-C6	120.2(10)
N2-C14-C16	108.3(2)	N1-C7-C8	108.34(18)	N1-C2-C1	108.6(2)
N2-C14-C11	110.3(2)	N1-C7-C5	110.23(18)	N1-C2-C3	110.4(2)
N1-C7-C4	110.3(2)	N2-C15-C13	110.18(17)	N2-C10-C11	110.2(2)
N1-C7-C15	109.4(2)	N2-C15-C16	109.21(19)	N2-C10-C9	109.6(3)

Table S4. Crystallographic data and structure refinement details for ***R*-F**, ***S*-F** and ***rac*-F**.

Identification code	***R*-F**	***S*-F**	***rac*-F**
Empirical formula	$C_{16}H_{22}Cl_6F_2N_2Sn$	$C_{16}H_{22}Cl_6F_2N_2Sn$	$C_{16}H_{20}Cl_6F_2N_2Sn$
Formula weight	611.74	611.74	611.74
Temperature/K	100	100	100
Crystal system	monoclinic	monoclinic	monoclinic
Space group	$P2_1$	$P2_1$	$P2_1/c$
a/Å	12.2505(2)	12.2157(11)	13.9427(7)
b/Å	7.16270(10)	7.1438(5)	7.1499(3)
c/Å	14.0193(2)	13.9697(15)	12.4112(6)
α/°	90	90	90
β/°	110.504(2)	110.521(11)	109.933(5)
γ/°	90	90	90
Volume/Å^3	1152.21(3)	1141.73(19)	1163.14(10)
Z	2	2	2
ρ_{calc}g/cm^3	1.763	1.779	1.747
μ/mm^{-1}	15.420	1.842	15.275
F(000)	604.0	604.0	604.0
Reflections collected	11681	17763	6707
Data/restraints/parameters	4590/1/248	5641/1/248	2338/0/126
Goodness-of-fit on F^2	1.054	1.072	1.074
Final R indexes [I>=2σ (I)]	R_1 = 0.0412, wR_2 = 0.1098	R_1 = 0.0209, wR_2 = 0.0481	R_1 = 0.0502, wR_2 = 0.1339
Final R indexes [all data]	R_1 = 0.0417, wR_2 = 0.1101	R_1 = 0.0222, wR_2 = 0.0486	R_1 = 0.0543, wR_2 = 0.1370
Flack parameter	-0.016(6)	-0.019(11)	1.043
CCDC	2207679	2207678	2210697

Table S5. Selected bond lengths (Å) for ***R*-F**, ***S*-F** and ***rac*-F**.

***R*-F**		***S*-F**		***rac*-F**	
Sn1-Cl5	2.4632(16)	Sn1-Cl5	2.3997(9)	Sn1-Cl5	2.4200(11)
Sn1-Cl3	2.4313(16)	Sn1-Cl6	2.4162(8)	Sn1-Cl5[a]	2.4200(11)
Sn1-Cl1	2.4232(13)	Sn1-Cl2	2.4301(8)	Sn1-Cl6	2.4201(12)
Sn1-Cl6	2.4080(16)	Sn1-Cl1	2.4051(9)	Sn1-Cl6[a]	2.4201(12)
Sn1-Cl4	2.4358(13)	Sn1-Cl4	2.4568(8)	Sn1-Cl4	2.4315(12)
Sn1-Cl2	2.4054(16)	Sn1-Cl3	2.4291(8)	Sn1-Cl4[a]	2.4315(12)
N1-C7	1.500(8)	N2-C10	1.505(4)	N1-C2	1.482(7)
N2-C16	1.521(7)	N1-C7	1.515(4)	F1-C6	1.356(7)
F1-C2	1.360(8)	F2-C14	1.362(4)		
F2-C10	1.366(9)	F1-C2	1.363(4)		

Symmetrical code for (*rac*-FMBA)$_2$SnCl$_6$: [a] 1-X, 1-Y, 1-Z;

Table S6. Selected bond angles (°) for ***R*-F**, ***S*-F** and ***rac*-F**.

***R*-F**		***S*-F**		***rac*-F**	
Cl3-Sn1-Cl5	89.79(6)	Cl5-Sn1-Cl6	90.66(3)	Cl5-Sn1-Cl5[a]	180.0
Cl3-Sn1-Cl4	87.47(6)	Cl5-Sn1-Cl2	177.06(3)	Cl5[a]-Sn1-Cl6[a]	90.95(4)
Cl1-Sn1-Cl5	90.49(6)	Cl5-Sn1-Cl1	92.75(3)	Cl5-Sn1-Cl6[a]	89.05(4)
Cl1-Sn1-Cl3	90.59(6)	Cl5-Sn1-Cl4	87.47(3)	Cl5[a]-Sn1-Cl6	89.05(4)

Cl1-Sn1-Cl4	177.94(5)	Cl5-Sn1-Cl3	91.31(3)	Cl5-Sn1-Cl6	90.95(4)
Cl6-Sn1-Cl5	87.51(6)	Cl6-Sn1-Cl2	90.65(3)	Cl5-Sn1-Cl4	91.33(4)
Cl6-Sn1-Cl3	177.04(7)	Cl6-Sn1-Cl4	90.50(3)	Cl5-Sn1-Cl4[a]	88.67(4)
Cl6-Sn1-Cl1	90.65(6)	Cl6-Sn1-Cl3	177.87(3)	Cl5[a]-Sn1-Cl4	88.67(4)
Cl6-Sn1-Cl4	91.26(6)	Cl2-Sn1-Cl4	89.89(3)	Cl5[a]-Sn1-Cl4[a]	91.33(4)
Cl4-Sn1-Cl5	88.82(6)	Cl1-Sn1-Cl6	90.21(3)	Cl6-Sn1-Cl6[a]	180.0
Cl2-Sn1-Cl5	179.14(7)	Cl1-Sn1-Cl2	89.87(3)	Cl6[a]-Sn1-Cl4	90.20(4)
Cl2-Sn1-Cl3	89.92(6)	Cl1-Sn1-Cl4	179.26(4)	Cl6-Sn1-Cl4[a]	90.20(4)
Cl2-Sn1-Cl1	90.33(6)	Cl1-Sn1-Cl3	90.49(4)	Cl6[a]-Sn1-Cl4	89.80(4)
Cl2-Sn1-Cl6	92.76(5)	Cl3-Sn1-Cl2	87.35(3)	Cl6-Sn1-Cl4	89.80(4)
Cl2-Sn1-Cl4	90.36(7)	Cl3-Sn1-Cl4	88.79(3)	Cl4-Sn1-Cl4[a]	180.0
C11-C10-F2	118.4(9)	C13-C14-F2	119.1(4)	C7-C6-F1	118.8(7)
C15-C10-F2	118.7(8)	C15-C14-F2	118.3(4)	C5-C6-F1	118.5(5)
C3-C2-F1	119.1(7)	C3-C2-F1	119.4(4)	N1-C2-C3	112.2(3)
C1-C2-F1	118.4(8)	C1-C2-F1	117.9(4)	N1-C2-C1	109.5(3)
N1-C7-C5	110.9(5)	N2-C10-C9	109.8(4)		
N1-C7-C8	108.3(6)	N2-C10-C11	118.8(4)		
N2-C16-C17	109.2(5)	N1-C7-C8	110.3(4)		
N2-C16-C13	109.5(5)	N1-C7-C5	113.6(4)		

Supplementary Figures

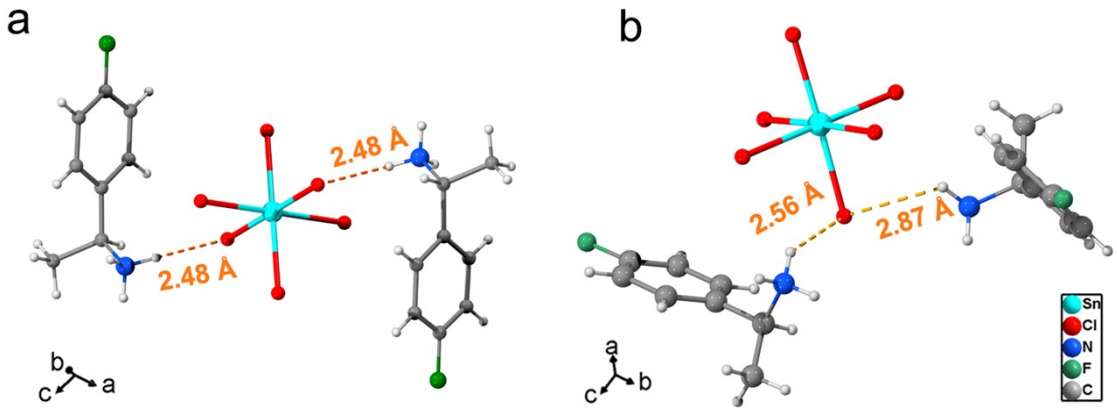

Figure S1. Crystal structures of (a) ***rac*-F** and (b) ***S*-F**. N−H···Cl−Sn hydrogen bonding interactions between the organic cation and inorganic scaffolds are marked by the dotted orange lines.

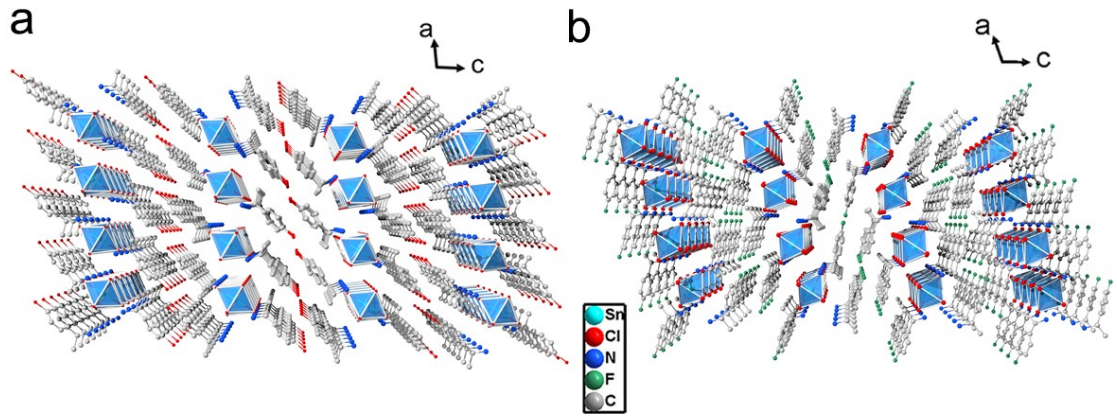

Figure S2. View of packing framework of (a) ***S*-Cl** and (b) ***S*-F**.

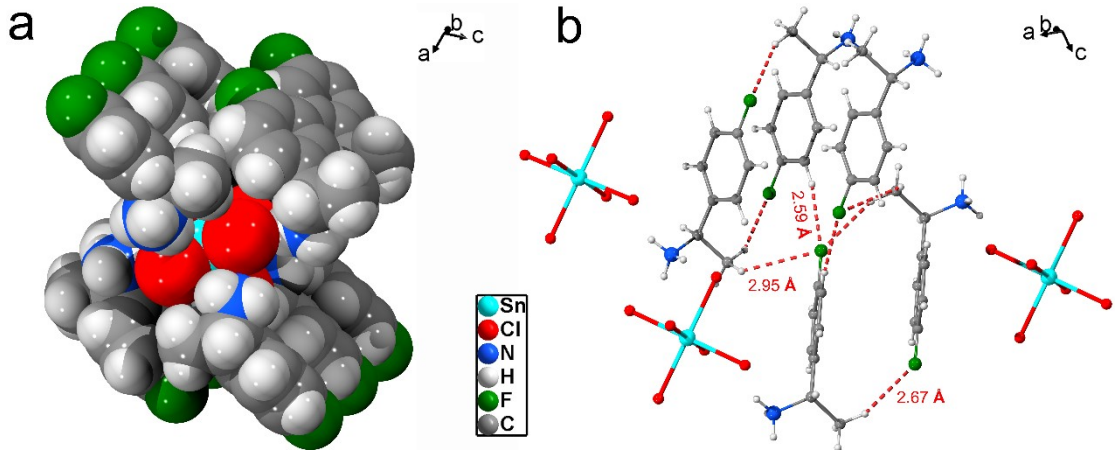

Figure S3. (a) Core–shell structure and (b) multiple C−H···F hydrogen bonding interactions of ***S*-F**.

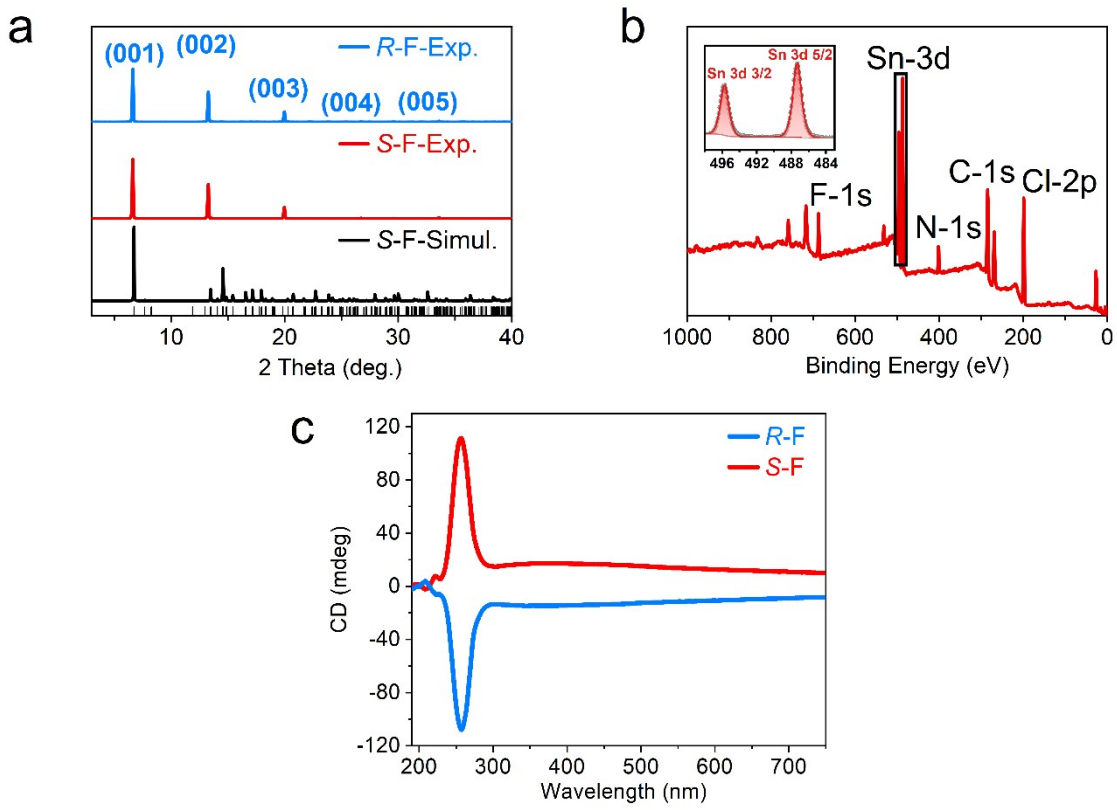

Figure S4. PXRD patterns of (a) ***R***-/***S***-**F**. (b) XPS survey scans of ***S***-**F**. Inset: High resolution XPS spectra and peak fitting for Sn 3d. (c) CD spectra of ***R***-/***S***-**F**.

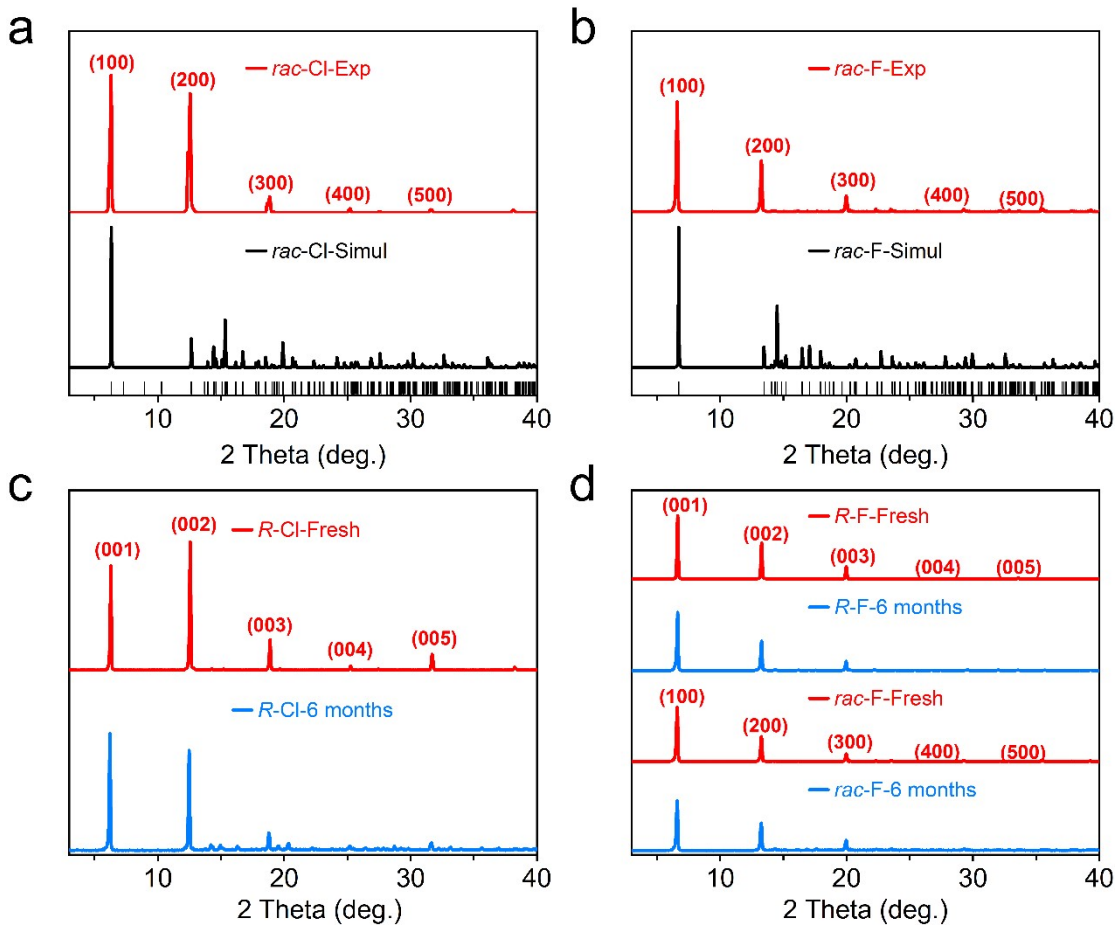

Figure S5. (a) PXRD patterns of ***rac*-Cl**, (b) ***rac*-F**. PXRD patterns of (c) ***R*-Cl**, (d) ***R*-/*rac*-F** recorded at same time interval from the day one of synthesis.

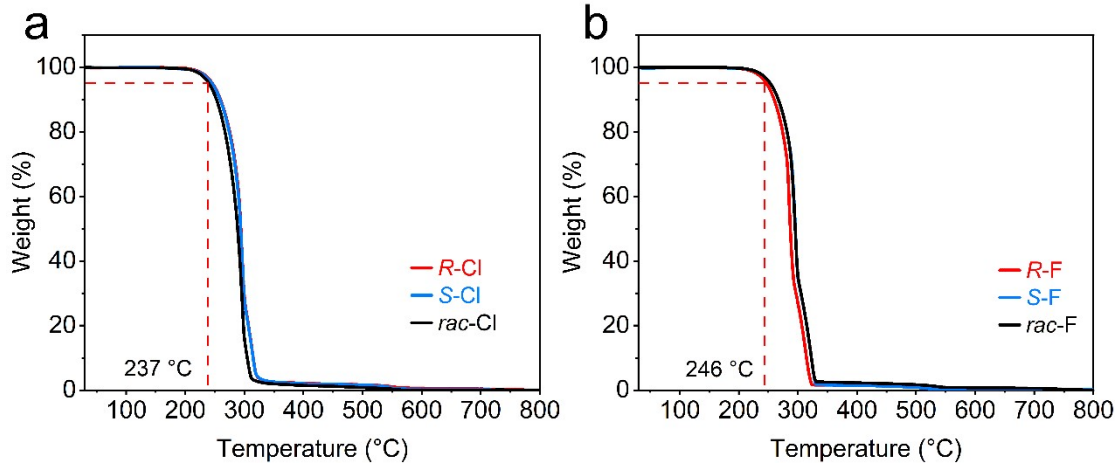

Figure S6. Thermal stability of (a) ***R*-/*S*-/*rac*-Cl** and (b) ***R*-/*S*-/*rac*-F**.

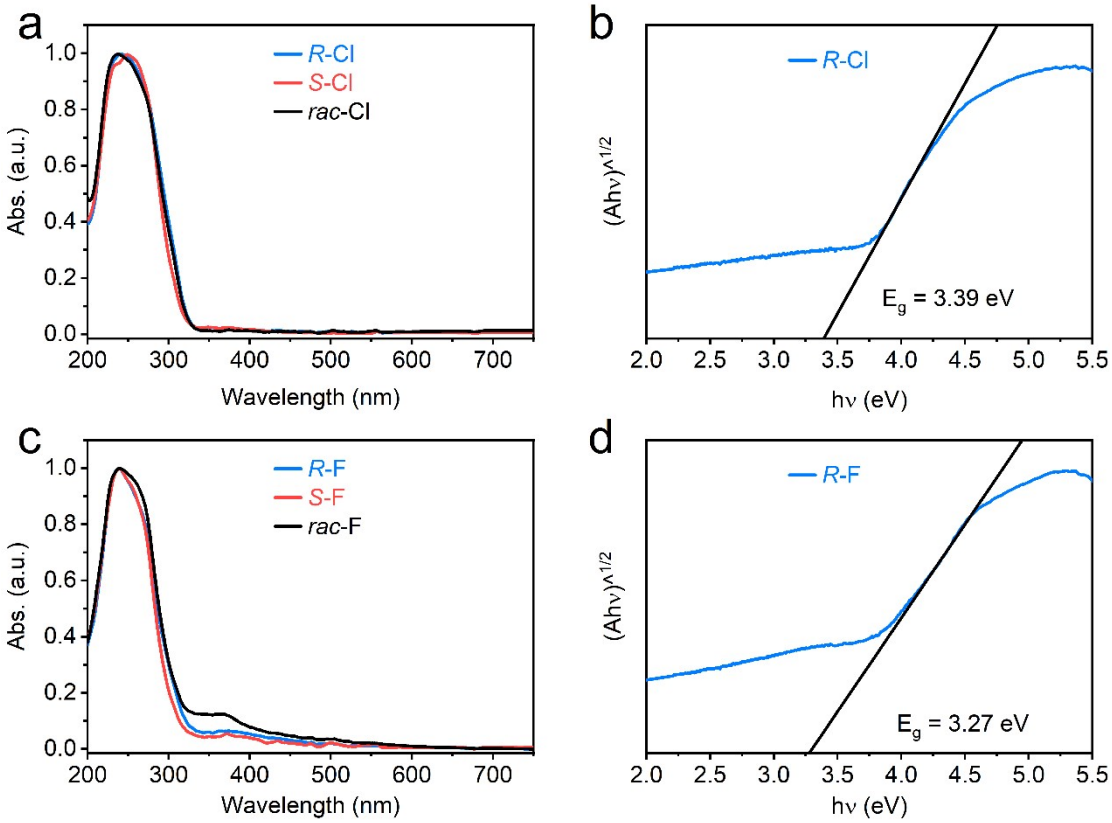

Figure S7. (a) Absorption spectra of ***R***-/***S***-/***rac***-**Cl**. (b) The optical bandgap of ***R***-**Cl** calculated from corresponding Tauc plot. (c) Absorption spectra of ***R***-/***S***-/***rac***-**F**. (d) The optical bandgap of ***R***-**F** calculated from corresponding Tauc plot.

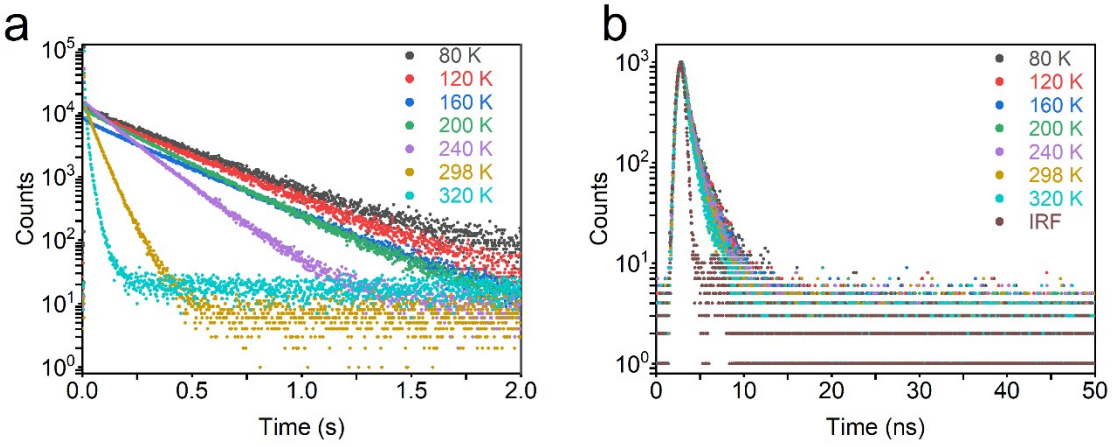

Figure S8. Photoluminescence decay profiles of ***rac***-**F** at (a) 398 nm and (b) 516 nm from 80–320 K.

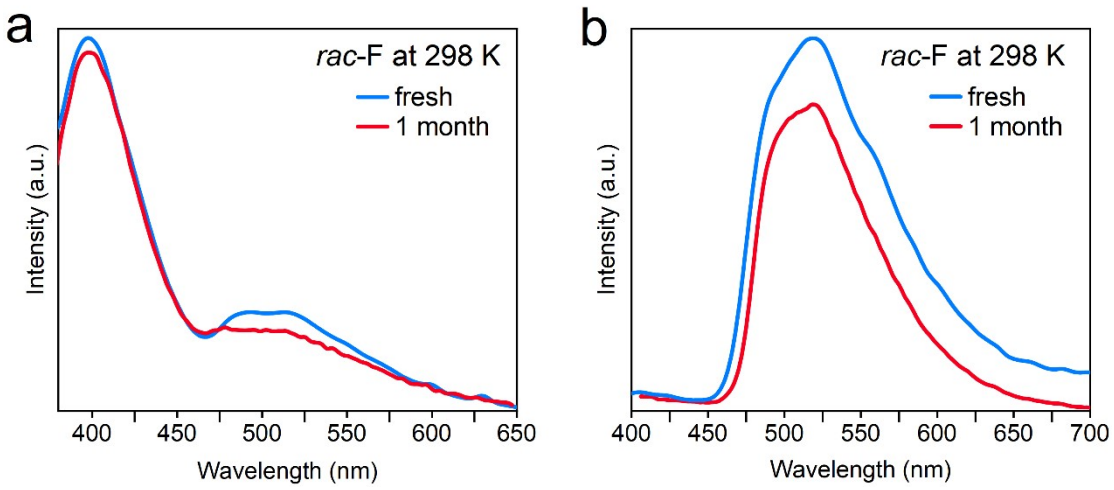

Figure S9. (a) Prompt and (b) delayed PL spectra of fresh ***rac*-F** sample and the one exposed in ambient atmosphere over one month.

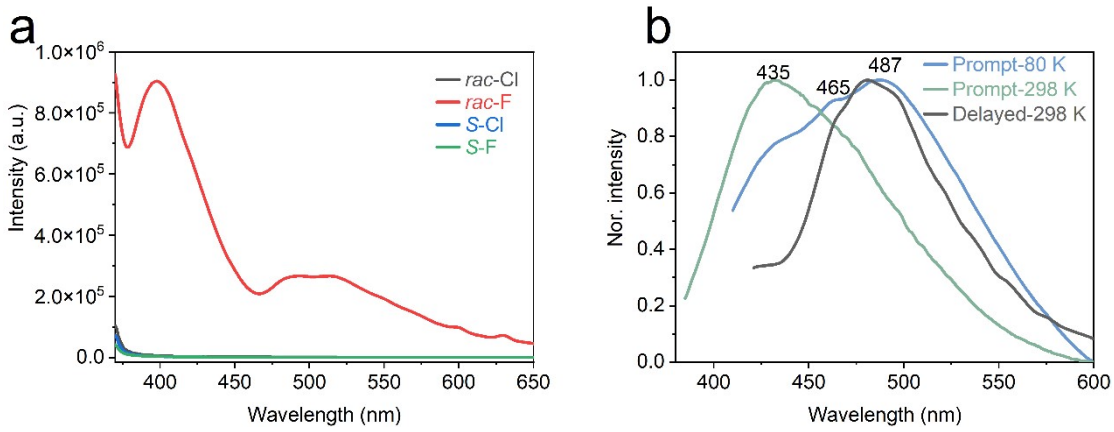

Figure S10. (a) Prompt PL spectra of ***rac*-F** and other Sn halides at the same test condition. (b) Normalized prompt and delay PL spectra of *rac*-FMBA-HCl.

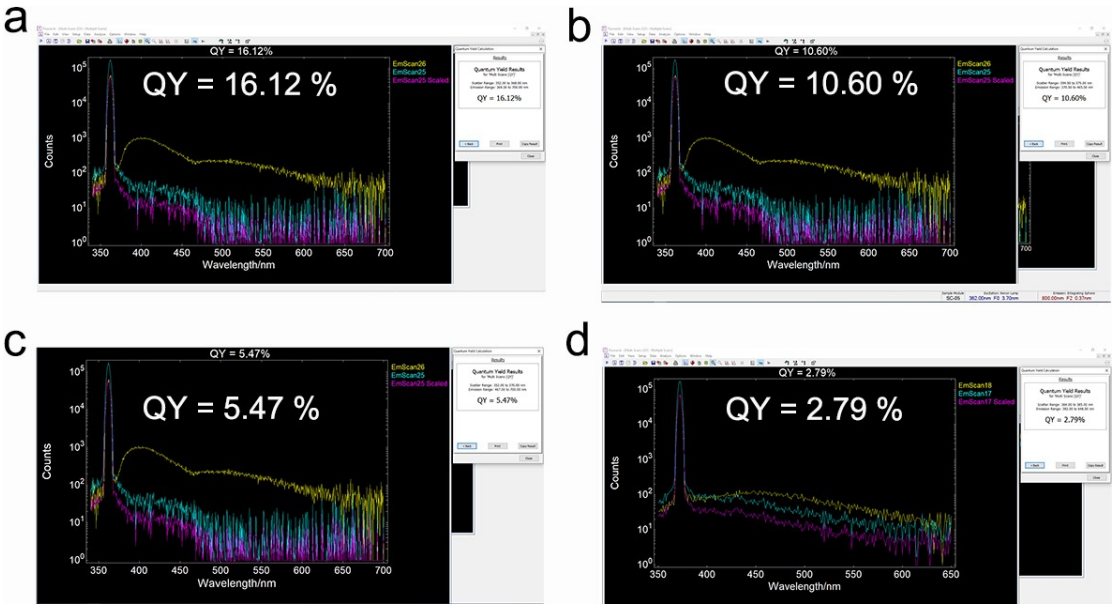

Figure S11. The (a) total PL quantum yield, (b) fluorescence quantum yield, (c) phosphorescence quantum yield of ***rac*-F**, and (d) total PL quantum yield of *rac*-FMBA-HCl.

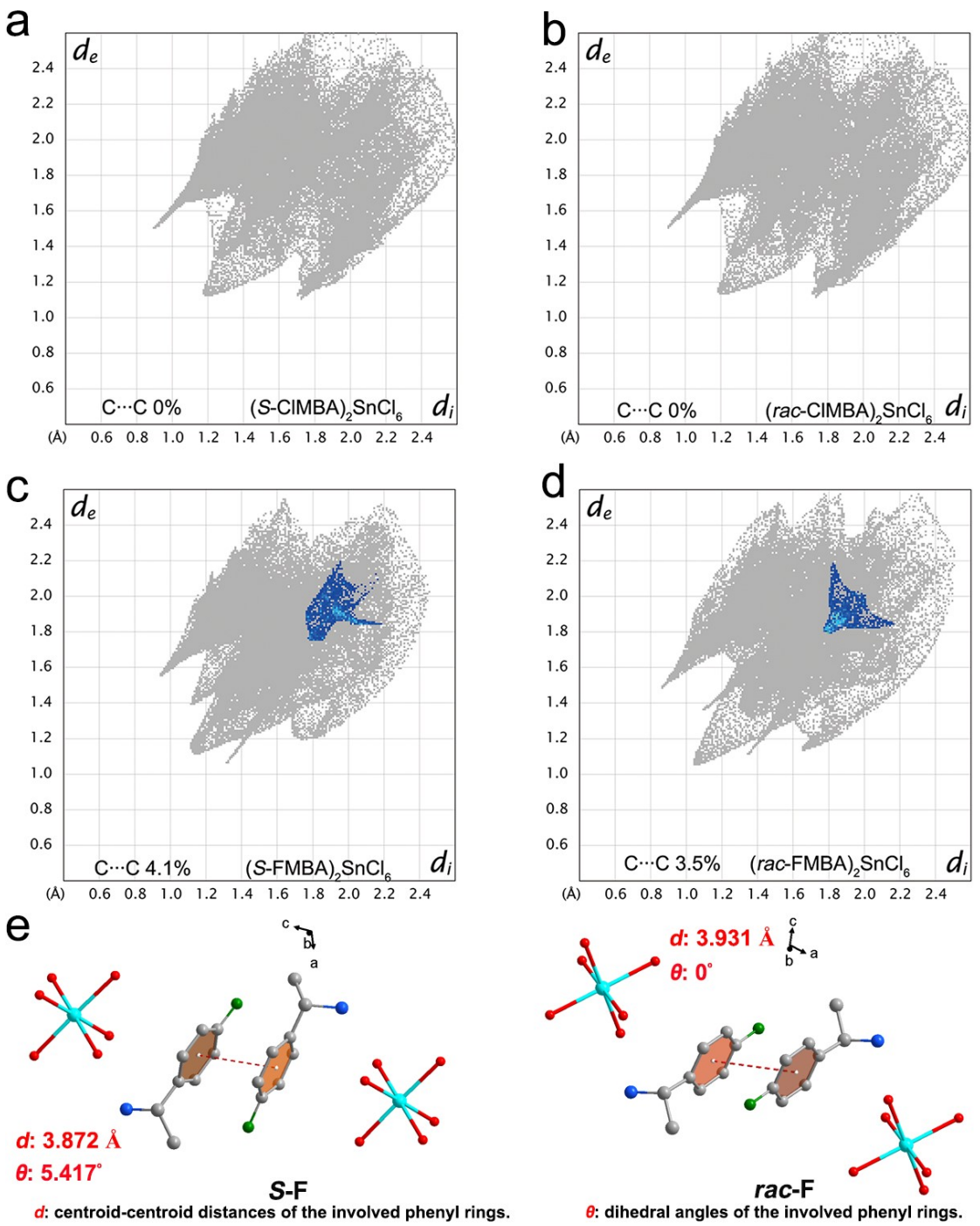

Figure S12. (a-d) 2D fingerprint plots. (e) π–π interactions of the involved phenyl rings in the ***S*-F** and ***rac*-F** crystals. Insert: d_i is the distance between the Hirshfeld surface and the nearest atom inside the Hirshfeld surface, while d_e is the distance between the Hirshfeld surface and the nearest atom outside the Hirshfeld surface. The intense of the color in the fingerprint plots represents the contribution of a pair (d_i, d_e) on the Hirshfeld surface; d: centroid-centroid distances of the involved phenyl rings; θ: dihedral angles of the involved rings.

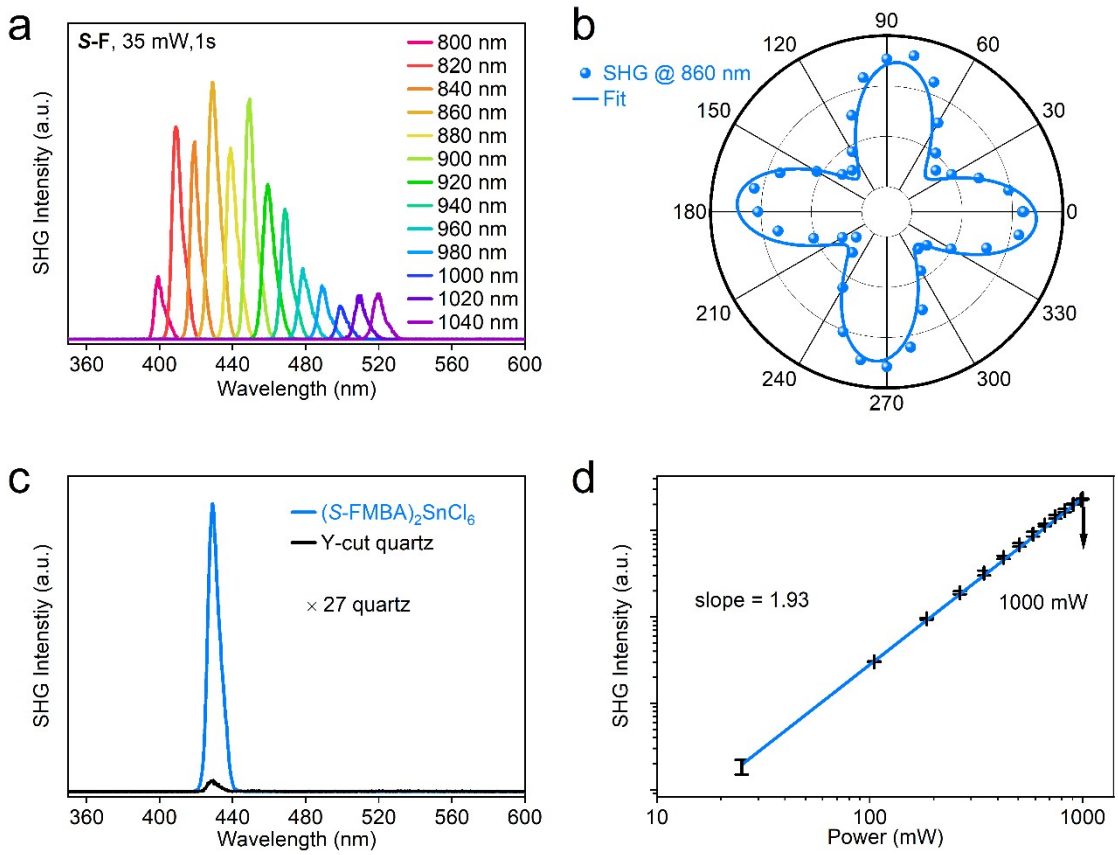

Figure S13. (a) NLO spectra of the ***S*-F** crystal pumped at various wavelengths. (b) Polarization dependence of the SHG intensity from a vertical oriented ***S*-F** crystal as function of the linear polarization angle. The polarization ratio up to 70.8%. Excitation and detection wavelengths are 860 and 430 nm, respectively (c) The comparison of SHG signal intensities of ***S*-F** and quartz at 860 nm under the same test conditions. (d) Logarithmic plot of SHG intensity as function of the incident power. The solid line is a linear fit with a slope of ~1.93.

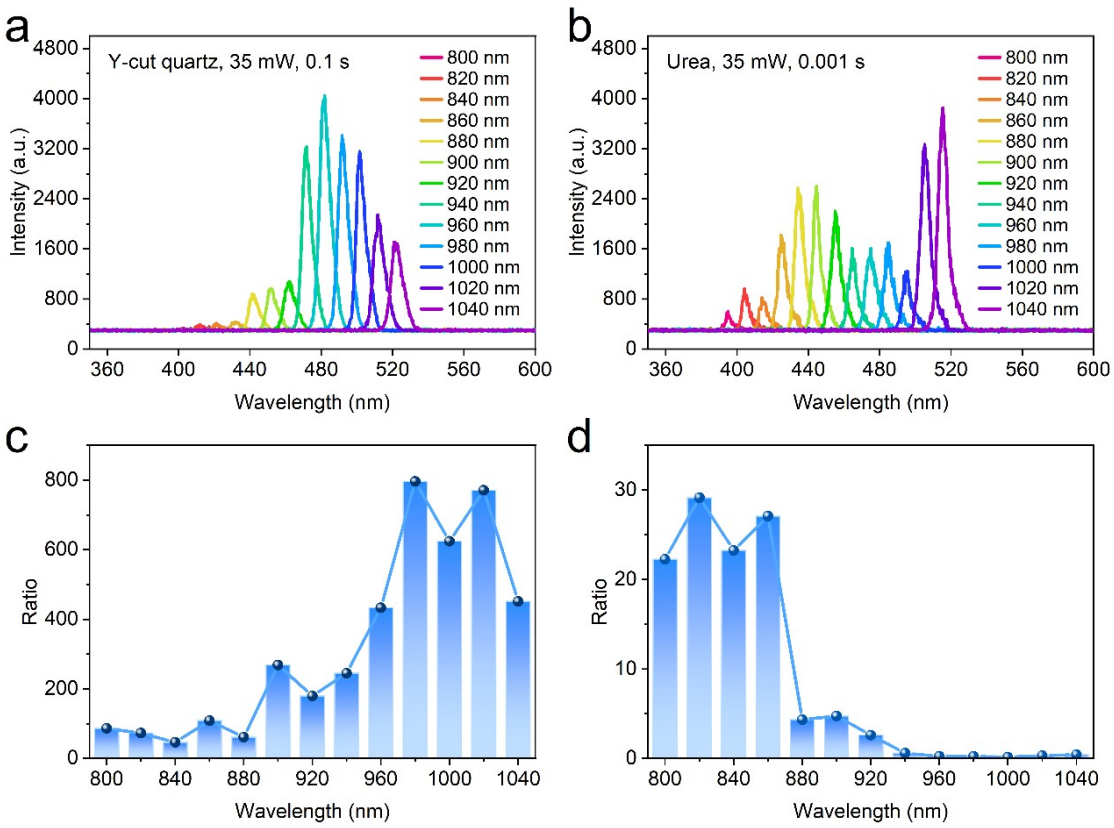

Figure S14. The SHG spectra of (a) Y-cut quartz and (b) urea at different wavelengths. The SHG intensity ratio of (c) ***S*-Cl** to Y-cut quartz and (d) ***S*-F** to Y-cut quartz.

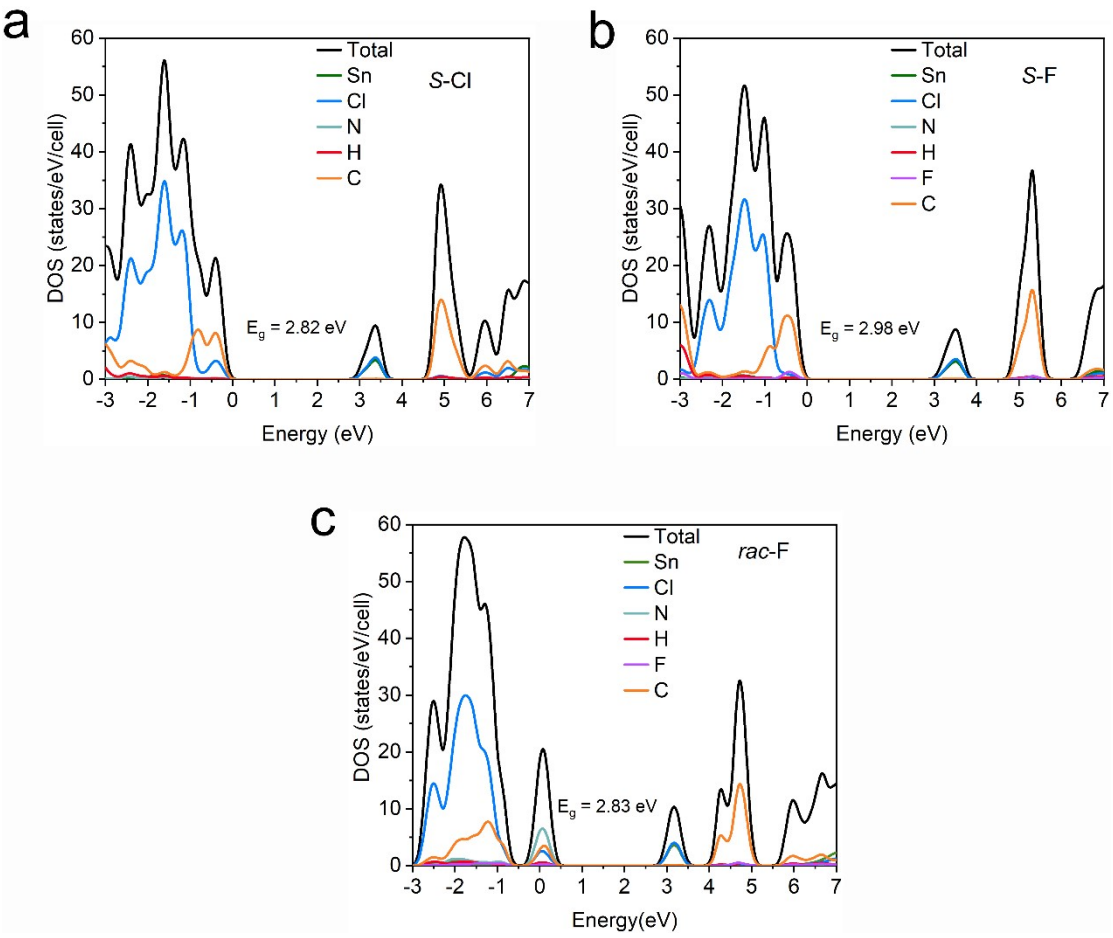

Figure S15. DOS of (a) ***S*-Cl**, (b) ***S*-F** and (c) ***rac*-F** projected on the constituent elements.

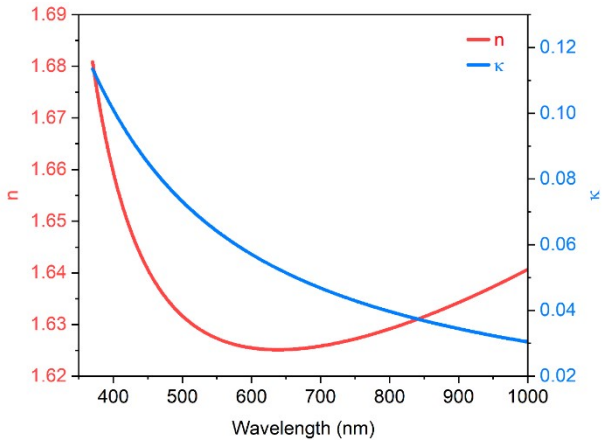

Figure S16. Refractive index (n) and extinction coefficient (κ) values of ***S*-Cl**.

Supplementary References

1 O. V. Dolomanov, L. J. Bourhis, R. J. Gildea, J. A. K. Howard and H. Puschmann, *J. Appl. Crystallogr.*, 2009, **42**, 339-341.
2 G. Kresse and J. Furthmüller, *Phys. Rev. B*, 1996, **54**, 11169-11186.
3 G. Kresse and D. Joubert, *Phys. Rev. B* 1999, **59**, 1758-1775.
4 J. P. Perdew, K. Burke and M. Ernzerhof, *Phys. Rev. Lett.*, 1996, **77**, 3865-3868.
5 J. Klimeš, D. R. Bowler and A. Michaelides, *Phys. Rev. B*, 2011, **83**, 195131.
6 J. Heyd and G. E. Scuseria, *J. Chem. Phys.*, 2004, **121**, 1187-1192.
7 A. Hermans, *Low-Temperature Processed Thin Films of Second-Order Nonlinear Optical Materials for Silicon Nitride Photonic Integrated Circuits*, Ghent University, Faculty of Engineering and Architecture, 2019.
8 S. Semin, X. Li, Y. Duan and T. Rasing, *Adv. Opt. Mater.*, 2021, **9**, 2100327.